

Lissajous rocking ratchet

Sergey Platonov,¹ Bernd Kästner,² Hans W. Schumacher,² Sigmund Kohler,³ and Stefan Ludwig^{1,*}

¹*Center for NanoScience & Fakultät für Physik, LMU-Munich, 80539 München, Germany*

²*Physikalisch-Technische Bundesanstalt, Bundesallee 100, 38116 Braunschweig, Germany*

³*Instituto de Ciencia de Materiales de Madrid, CSIC, 28049 Madrid, Spain*

(Dated: March 16, 2015)

Breaking time-reversal symmetry (TRS) in the absence of a net bias can give rise to directed steady-state non-equilibrium transport phenomena such as ratchet effects. Here we present, theoretically and experimentally, the concept of a Lissajous rocking ratchet as an instrument based on breaking TRS. Our system is a semiconductor quantum dot (QD) with periodically modulated dot-lead tunnel barriers. Broken TRS gives rise to single electron tunneling current. Its direction is fully controlled by exploring frequency and phase relations between the two barrier modulations. The concept of Lissajous ratchets can be realized in a large variety of different systems, including nano-electrical, nano-electromechanical or superconducting circuits. It promises applications based on a detailed on-chip comparison of radio-frequency signals.

PACS numbers: 73.63.Kv, 05.60.-k, 85.35.Gv

Ratchets cause directed particle motion due to a combination of broken symmetry and non-equilibrium forces, where the latter may be deterministic or fluctuating. The most famous example is Feynman's *flashing ratchet* which uses a pulsating spatially asymmetric potential to actively turn fluctuations into work [1–4]. Another species is the *rocking ratchet* driven by forces periodic in time but with broken spatio-temporal symmetry. A simple example of a rocking ratchet is a pump which transports electrons one-by-one through a QD driven by two external periodic forces with a relative phase breaking the symmetry [5, 6]. This is in contrast to the somewhat simpler turnstile where the spatial symmetry is broken by a finite dc voltage [7]. In the non-adiabatic limit electron pumps are investigated for their suitability as current standard [8, 9].

In this article we restrict ourselves to the adiabatic regime and study a generic implementation of a rocking ratchet by applying two time-periodic forces, phase-locked at various commensurate frequencies. In our implementation we measure the dc current I through a QD embedded in the two-dimensional electron system (2DES) 90 nm beneath the surface of an etched 1 μm wide channel of GaAs/AlGaAs heterostructure. The 2DES is cooled to $\sim 100\text{ mK}$ where its carrier density is $n_e \simeq 2.83 \times 10^{15}\text{ m}^{-2}$ and its mobility is $\mu_e \simeq 320\text{ m}^2\text{ V}^{-1}\text{ s}^{-1}$. We control the QD by applying voltages to two metal gates [see lower inset in Fig. 1(a)].

For a first orientation we present in Fig. 1(a) a stability diagram of our QD measured at finite dc voltage $V = (\mu_R - \mu_L)/e = 100\text{ }\mu\text{V}$ applied between its two leads (at chemical potentials $\mu_{L,R}$). Plotted is the current I as a function of gate voltages \tilde{V}_L and \tilde{V}_R applied to the left (L) versus right (R) gate [yellow in the rhs inset of Fig. 1(a)]. The axes $\tilde{V}_{L,R}$ are offset relative to the actually applied voltages, such that $\tilde{V}_L = \tilde{V}_R = 0$ at our working point, which is marked in Fig. 1(a) by a black

cross. We define the chemical potential μ_n of the QD as the energy needed to add the next electron to it, where n is an index number and we choose $n = 0$ for the dot level closest to the working point. For $\mu_R \gtrsim \mu_n \gtrsim \mu_L$ the Coulomb blockade is lifted and a current I flows along broadened lines oriented perpendicular to the bisecting line (dashed line). With increasing $\tilde{V}_{L,R}$, the barriers coupling the QD to both leads shrink causing I to grow. At the bisecting line, the QD is symmetrically coupled to both leads but with increasing distance, one barrier shrinks and the other one grows, causing I to decrease.

We parametrize the QD by its dot-lead tunnel rates $\Gamma_{L,R}$ and its charging energies $E_C(n) = \mu_n - \mu_{n-1}$, where at our working point, $E_C(0) \equiv E_C^0 \simeq 1.27\text{ meV}$. Exploring a limited range of the stability diagram the capacitive coupling between gates and the QD can be modeled by the linear relation $\mu_n = \mu_n^0 - \kappa_\mu(\tilde{V}_L + \tilde{V}_R)$ with $\kappa_\mu \simeq 0.38e$. Here e is the elementary charge and μ_n^0 are the chemical potentials for $\tilde{V}_L = \tilde{V}_R = 0$. The tunnel couplings $\Gamma_L(\tilde{V}_L)$ and $\Gamma_R(\tilde{V}_R)$ are controlled by the respective gate voltages $V_{L,R}$, where we neglect the very weak cross couplings $\Gamma_L(\tilde{V}_R)$ and $\Gamma_R(\tilde{V}_L)$. The $\Gamma_{L,R}(\tilde{V}_{L,R})$ are determined by fitting a theoretical prediction to the current in Fig. 1(a). Our calibrations are detailed in the Supplemental Material, Ref. [10]. In the following we define rocking ratchets by making use of the mutually coupled dependencies of $\Gamma_{L,R}$ and μ_n on both gate voltages.

To break the TRS, we periodically modulate $\tilde{V}_L(t)$ and $\tilde{V}_R(t)$ such that they define trajectories along Lissajous figures centered at the working point:

$$\vec{v}_{k,\phi}(t) = \begin{pmatrix} \tilde{V}_L(t) \\ \tilde{V}_R(t) \end{pmatrix} = A \begin{pmatrix} \cos(2\pi ft - \phi) \\ \cos(k2\pi ft) \end{pmatrix}, \quad (1)$$

where, for simplicity, we restrict ourselves to integer frequency ratios k . We prepare the two modulation am-

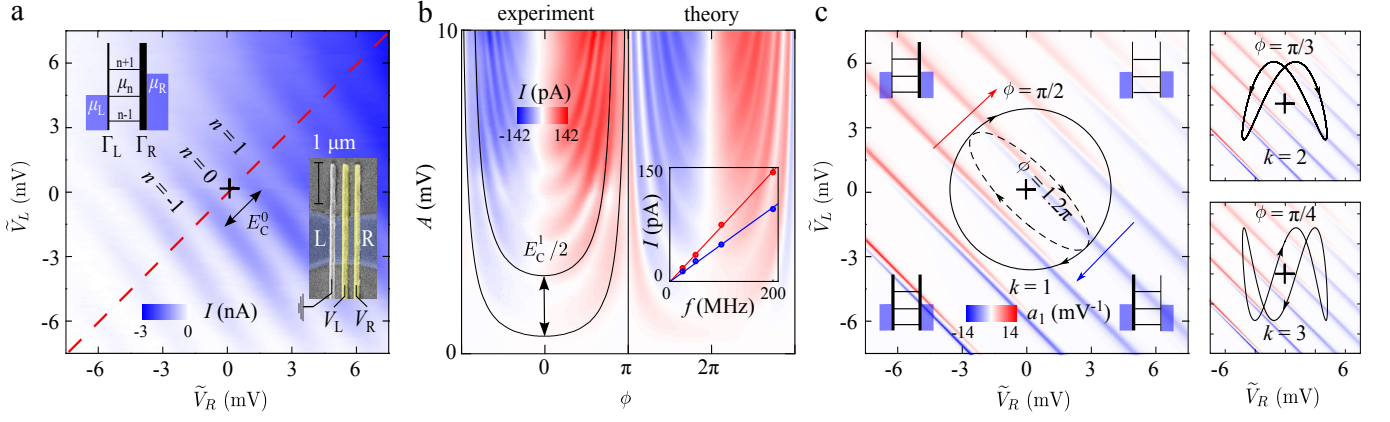


FIG. 1. (a) Current I through the QD as function of gate voltages $\tilde{V}_{L,R}$ in response to a dc voltage $V = (\mu_R - \mu_L)/e = 100 \mu\text{V}$. A double arrow indicates the charging energy E_C^0 at the working point (black cross). Lower inset: scanning electron microscope image of the sample. The wafer is etched at the gray area, only the blue channel contains 2DES. Two Ti/Au gates (yellow) are used to define a QD, a third gate (gray) is electrically grounded. Upper inset: QD sketch; vertical lines are electrostatic barriers with tunnel couplings $\Gamma_{L,R}$ controlled by gate voltages. Horizontal lines are chemical potentials μ_n of the QD, blue areas indicate occupied states in the degenerate leads at chemical potentials $\mu_{L,R}$. (b) $\tilde{V}_{L,R}$ are modulated according to Eq. (1), both with frequency $f = 200 \text{ MHz}$ ($k = 1$). Measured (left) versus calculated (right, $V = 1 \mu\text{V}$) current I versus modulation amplitude and phase. Inset: measured $I(f)$ at $A = 9 \text{ mV}$ for the two phases $\phi \simeq 0.3\pi$ (blue), $\phi \simeq 0.6\pi$ (red). (c) Vector field \vec{a} (explained in text and Ref. [10]) versus gate voltages and typical Lissajous trajectories for $k = 1, 2, 3$ according to Eq. (1). Black crosses mark the working point, QD sketches indicate relative strengths of tunnel couplings to the leads.

plitudes to be identical, A . The trajectories can cross several charging lines of the stability diagram.

Our first experiment resembles an adiabatic electron pump defined by Eq. (1) with $k = 1$, i.e. identical frequencies. Figure 1(b) compares a typical measurement (lhs) with model predictions (rhs), both for $f = 200 \text{ MHz}$ and $\mu_L \simeq \mu_R$. The current, plotted as a function of A and phase ϕ , displays clear resonances following lines of constant $A \cos(\phi/2)$ (solid lines). These resonances indicate discrete current contributions of the n -electron QD levels separated by $\kappa_\mu \Delta A = E_C(n)/2$, where the factor 2 accounts for two gates being modulated. During each pumping cycle approximately $\text{int}(2A\kappa_\mu/E_C^0)$ ground state levels fulfill $\mu_n(t) = \mu_{L,R}$ twice. For $f \leq 200 \text{ MHz}$ we find $I \propto f$ at fixed ϕ and A [inset in Fig. 1(b)] which confirms that we operate in the adiabatic regime, where the QD is always in its momentary ground state and the charge transferred across it per cycle is constant [10]. Each QD level is unoccupied whenever $\mu_n(t) > \mu_{L,R}$ and its n -electron ground state is occupied for $\mu_n(t) < \mu_{L,R}$. Whenever $\mu_n(t) \simeq \mu_{L,R}$ an electron tunnels into the QD if $d\mu_n/dt < 0$ and out of the QD if $d\mu_n/dt > 0$. With which lead the electron is thereby exchanged depends on ϕ and the ratio Γ_L/Γ_R , which is modulated in time, see Eq. (1) and above.

This scenario resembles a rocking ratchet [4] where the current changes direction at $\phi = 0, \pi$, independent of k . For $k = 1$ it gives rise to the two-fold symmetry of a pump observed in Fig. 1(b). The symmetry can be compromised for four reasons (independent of k): (i) dissipation by transitions within the QD's excitation spectrum.

This, however, would go along with non-adiabaticity which we already excluded [inset in Fig. 1(b)]; (ii) a spatially asymmetric local disorder potential which influences the ratio Γ_L/Γ_R as function of n , depending on the electronic probability distribution. This is ignored in our model but can explain deviations to the measured current, particularly near $\phi = 0$ where the QD's chemical potentials $\mu_n(t)$ are modulated strongest and additional spatial disorder causes rectification [11]; (iii) the n -dependence of the charging energy and the choice of the working point; (iv) a dc voltage between the leads ($V \neq 0$). Points (iii) and (iv) are included in our model and discussed below.

A formal description of the general case for any integer k including different frequencies modulating the two gates, is detailed in Ref. [10] and can be summarized as follows: We start from an expression for the current through the time-periodic system obtained with Floquet transport theory [12, 13]. Taylor expansion up to first order in Ω provides the adiabatic limit of the dc current:

$$I = \bar{G}V + Q^{\text{cycle}}f + I^{\text{rect}}, \quad (2)$$

which can be traced back to the transport properties of the time-independent system for the parameters along the trajectory $\vec{v}_{k,\phi}(t)$, defined in Eq. (1). The first term of Eq. (2) contains the time-averaged conductance of the QD, \bar{G} . It can be understood as dc current which flows whenever any resonance fulfills the condition $\mu_L \lesssim \mu_n \lesssim \mu_R$ (or $\mu_R \lesssim \mu_n \lesssim \mu_L$). For the theory data in Fig. 1(b) we have used $V = 1 \mu\text{V}$ which provides good agreement with the measured data. This tiny dc volt-

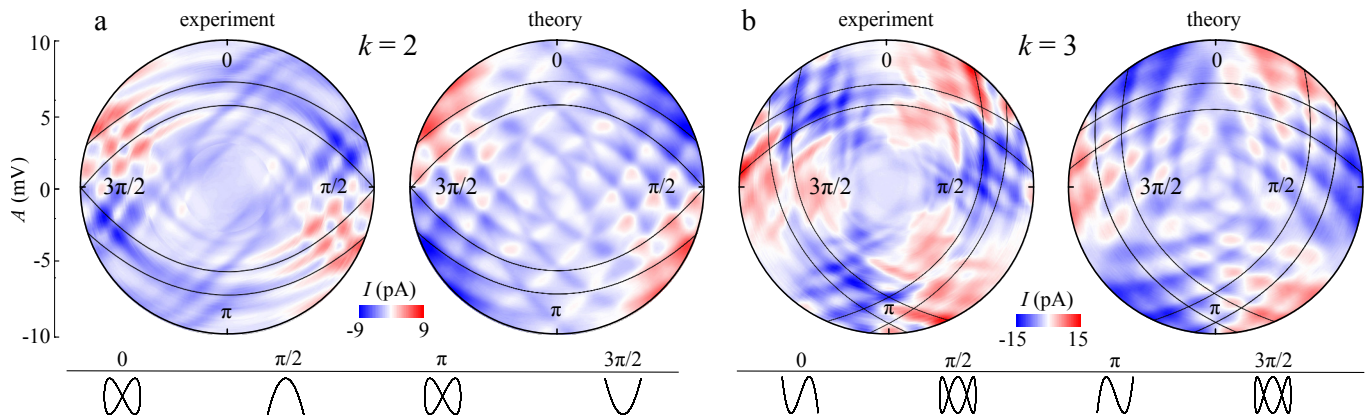


FIG. 2. Measured (left) and computed (right) current as a function of modulation amplitude A and phase difference ϕ between $V_L(t)$ and $V_R(t)$: (a) $V_L(t)$ at 50 MHz and $V_R(t)$ at 100 MHz ($k = 2$), see Eq. (1), and (b) at 50 MHz and 150 MHz ($k = 3$). Solid lines indicate the resonances $\mu_n \simeq \mu_{L,R}$ for $n = 3, 4$. Bottom: Lissajous figures for $k = 2$ and $k = 3$.

age is not purposely applied but caused by the current amplifier.

The second term of Eq. (2) is the dc current caused by the pumped charge, Q^{cycle} . This ratchet current can be expressed as a closed loop integral of a vector field $\vec{a}(\vec{v})$ [\vec{v} being defined in Eq. (1)], which follows from the scattering matrix [10]. Here, we restrict ourselves to a qualitative explanation and plot its component a_1 as a function of $\tilde{V}_{L,R}$ in Fig. 1(c); note that $|a_2| \simeq |a_1|$. $\vec{a}(\vec{v})$ vanishes unless $\mu_n \simeq \mu_{L,R}$ and, hence, marks the charging lines. Its direction relates to the ratio Γ_L/Γ_R : since $a_1 \simeq \pm a_2$, \vec{a} is either parallel or anti-parallel to the (1,1) direction in Fig. 1(c), depending on whether $\tilde{V}_L \gg \tilde{V}_R$ (implying $\Gamma_L \gg \Gamma_R$) or $\tilde{V}_L \ll \tilde{V}_R$.

The third contribution in Eq. (2), I^{rect} , stems from a tiny ac modulation of the lead chemical potentials induced by the capacitive coupling between each gate and its adjacent lead. The amplitude of the resulting ac source-drain voltage is of the order $0.1\mu\text{V}$ and, owing to the capacitive coupling, is phase-shifted by $-\pi/2$ with respect to the gate voltages. This phase shift between the ac bias and the time dependent QD conductance gives rise to dynamic rectification. I^{rect} turns out essential for the quantitative agreement between the measured currents and the theoretical predictions of our model. Interestingly, $I^{\text{rect}} \neq 0$ requires a phase shift between the two modulated gate voltages. As such, dynamic rectification is very different in nature than the usually and hitherto discussed rectification caused by static asymmetries of the geometry and I - V curve [14].

The symmetries of these three contributions as a function of ϕ can be revealed by formally reverting time [10]. We find $2k$ symmetry points at which \bar{G} obeys TRS, while Q^{cycle} and I^{rect} are anti-symmetric under time reversal and, hence, under phase reflection.

Figure 1(c) contains example Lissajous figures $\vec{v}_{k,\phi}(t)$ for $\phi = \pi/(k+1)$: a circle for $k = 1$, a distorted figure eight for $k = 2$ and a triple loop for $k = 3$. For

$k = 1$ and ϕ slightly different from π , $\vec{v}_{k=1,\phi}(t)$ is an eccentric ellipse which corresponds to the pumping measurements already discussed in literature [5, 6] [dashed line in Fig. 1(c)]. Whenever $\vec{v}_{k,\phi}(t)$ crosses a charging line, the charge of the QD changes by one electron. If this happens in a red region corresponding to $a_1, a_2 > 0$ with $\Gamma_L > \Gamma_R$ an electron will be exchanged preferably with the left lead. In the blue region with $a_1, a_2 < 0$ and $\Gamma_L < \Gamma_R$, charge exchange with the right lead is preferred. We define $I > 0$ for electrons flowing from the right to the left. Then, crossing a blue area from above and a red area from below (see example for $k = 1$) both contribute to $I < 0$, each with half an electron charge per cycle. Our example for $k = 3$ also results in $I < 0$. For $k = 2$, the contributions of the outer loops to Q^{cycle} have opposite sign and, thus, cancel each other to some extent, despite that the curves have a different symmetry axis than the resonance lines. The same holds for the inner loops. Therefore, we expect the pump current for $k = 2$ to be generally smaller than for $k = 1$. For $k = 3$, by contrast, symmetry-related parts of each curve again contribute to Q^{cycle} with the same sign. A generalization of these arguments leads to the expectation that for even values of k , the pump current should be larger than for odd values. For larger k , however, there will be an increasing number of contributions with any sign and, thus, the situation becomes less clear.

In a realistic system, in addition, the symmetry of $\vec{a}(\vec{v})$ is compromised because of point (iii) above: the separation of charging lines, E_C , depends on n and our working point (see Fig. 1) is chosen to further decrease symmetry. As a result the contributions to Q^{cycle} from the outer loops for $k > 1$ do not completely cancel each other and we find a ratchet current for all k , specifically with deviations from integer Q^{cycle} for $k = 3, 5, 7, \dots$ and from $Q^{\text{cycle}} = 0$ for $k = 2, 4, 6, \dots$. The mapping $\phi \rightarrow -\phi$ should survive the compromised symmetry discussed above and still result in a reversal of the direc-

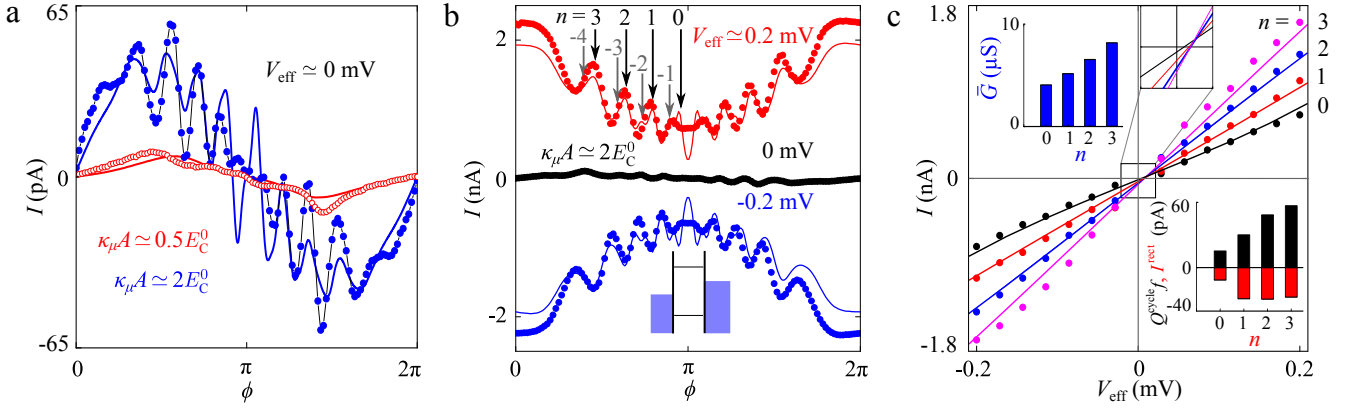


FIG. 3. Symbols are measured, lines depict theory. (a) $I(\phi)$ near zero bias for $\kappa_\mu A \simeq 2E_C^0$, $V_{\text{off}} \simeq -1 \mu\text{V}$ (blue) and $\kappa_\mu A \simeq 0.5E_C^0$, $V_{\text{off}} \simeq 0 \mu\text{V}$ (red); $k = 1$, $f = 100 \text{ MHz}$. (b) $I(\phi)$ for $\kappa_\mu A \simeq 2E_C^0$, $V_{\text{off}} \simeq 9 \mu\text{V}$ including curves at finite bias. Arrows indicate the phases at which the QD levels with indices n start to reach the transport window ($\mu_L \leq \mu_n \leq \mu_R$ or $\mu_R \leq \mu_n \leq \mu_L$) during each modulation period. The relative shift between $n = 0, -1$ and $n = 1, -2$, etc. is caused by our working point not being centered between two QD chemical potentials [see Fig. 1(a)]. (c) I - V_{eff} characteristics for $\kappa_\mu A \simeq 2E_C^0$, at current peaks near black arrows in (b). The maxima slightly shift proportional to $|V_{\text{eff}}|$. Upper right inset: magnification, theory lines intersect at $V_{\text{eff}} \simeq 9 \mu\text{V}$. Upper left inset: average conductance \bar{G} . Lower inset: I^{rect} (red, negative values) and pump current $Q^{\text{cycle}} f$ (black, positive), both being independent of V_{eff} .

tion of $\vec{v}_{k,\phi}(t)$ and, therefore, also in a current reversal. Furthermore, the current direction should possess the k -fold symmetry $\phi \rightarrow \phi + 2\pi/k$. As a pump has two-fold symmetry, the case of $k > 1$ goes qualitatively beyond the scope of a pump. For the $2k$ equally spaced phases $\phi = 0, \pi/k, \dots, (2k-1)\pi/k$, no charge is pumped at all, Q^{cycle} should change its sign and, thus, vanish. This symmetry is apparent albeit not perfect in Fig. 2 which compares the measured ratchet currents for $k = 2$ and $k = 3$ as function of the modulation amplitude and ϕ with model calculations. More values of k are available in Ref. [10]. To improve modeling of our measured data we included all experimentally known facts such as $E_C(n)$ and line broadening into the numeric calculations (see Ref. [10]). The best agreement is then reached if we additionally assume a dc voltage of $V \sim \pm 5 \mu\text{V}$. This is likely the voltage offset of the used high-precision current amplifier (input) which slowly drifts in time and is hard to control due to its dependence on the ambient temperature. Near the symmetry points of $Q^{\text{cycle}} = 0$, the symmetry of the overall current is markedly reduced by the dc-current $\bar{G}V$ in Eq. (2), point (iv) above [10].

In Fig. 3(a) we present measured versus predicted $I(\phi)$ -curves at $V_{\text{eff}} \simeq 0$ for two different modulation amplitudes. For accuracy we have introduced the effective voltage $V_{\text{eff}} = V + V_{\text{off}}$ corrected by the voltage offset, V_{off} , caused by the current amplifier. At $\phi = \pi$, Γ_L and Γ_R oscillate in anti-phase and the QD states μ_n are static (for all k and independent of A). The modulation of $\mu_n(t)$ grows with $|\phi - \pi|$ and with it the number of QD levels contributing to current, i.e. fulfilling $\mu_n(t) = \mu_{L,R}$ twice during each modulation period. Consequently, between $0 < \phi < \pi$ (equally for $\pi < \phi < 2\pi$) $|I(\phi)|$ in-

creases whenever another QD level starts to contribute to Q^{cycle} . For the smaller amplitude at most two levels with $n = -1, 0$, for the larger amplitude at most eight levels with $-4 \leq n \leq 3$, reach $\mu_n = \mu_{L,R}$ during each period and, hence, contribute to I . As ϕ approaches 0 or 2π the gate modulation becomes symmetric restoring TRS, hence I drops to zero [10]. The differences between theory and experiments in Fig. 3(a) are not fully understood, but could be related to the contribution of excited states, which are not accounted for in our model.

As V_{eff} is increased towards $|eV_{\text{eff}}| > E_C^0$ the dc contribution of the current $\bar{G}V_{\text{eff}}$ [first term of Eq. (2)] rapidly gains weight yielding a transition to axial mirror symmetry reflecting the phase independent current direction determined by the sign of V_{eff} . This is clearly visible in Fig. 3(b) where we include data for the larger amplitude at finite $V_{\text{eff}} \simeq \pm 0.2 \text{ mV}$. The approximately quadratic current increase (decrease) away from $\phi = \pi$ (or equivalently from $\phi = 0, 2\pi$) is related to the details of $\Gamma_{L,R}(t)$.

The symbols in Fig. 3(c) are the measured I - V_{eff} characteristics at the current maxima near black arrows in Fig. 3(b). Here $|V_{\text{eff}}| < E_C^0/2e$ so that only a single QD state contributes to I at any instance of time. In this regime we find approximately $I \propto V_{\text{eff}}$. Straight lines are the corresponding theory data which intersect as a common point at $V_{\text{eff}} \neq 0$. The theory data are composed of three contributions shown as bar charts: \bar{G} in blue, $Q^{\text{cycle}} f$ in black and I^{rect} in red. The fair agreement between theory and experiment confirms the theoretically assumed adiabaticity for our experiments.

In summary, we have realized a Lissajous rocking ratchet by modulating a single QD with two phase-locked voltage signals at commensurable frequencies. The di-

rectional motion is a consequence of breaking the TRS which, as our analysis revealed, is restored only for certain phases between the signals. To achieve this, it is not sufficient to modulate the QD-lead couplings but additional modulation of the QD levels via capacitive cross-couplings is essential. While our experiments used a semiconducting QD, similar rocking ratchets could be realized in different systems, such as superconducting circuits, nano-electromechanical systems or molecular electronics. Lissajous ratchets encode the relative phase, frequency and amplitude information of two radio frequency signals into a time averaged dc signal, in spirit similar to a Lock-In amplifier. The ability to compare rf-signals on the chip promises a refined level of control desired for applications related to on-chip spectrum analyzing or quantum information processing.

We thank Klaus Pierz for supplying the wafer material. We are grateful for financial support from the DFG via LU 819/4-1, SFB-631 and the Cluster of Excellence “Nanosystems Initiative Munich (NIM)” and by the Spanish Ministry of Economy and Competitiveness via grant No. MAT2011-24331. S.L. acknowledges support via a Heisenberg fellowship of the DFG.

Additional experiments

Experimental setup

The GaAs / AlGaAs wafer containing the QD sample was mounted on a radio frequency (rf) sample holder as shown in Fig. 4, such that the wafer was in direct contact

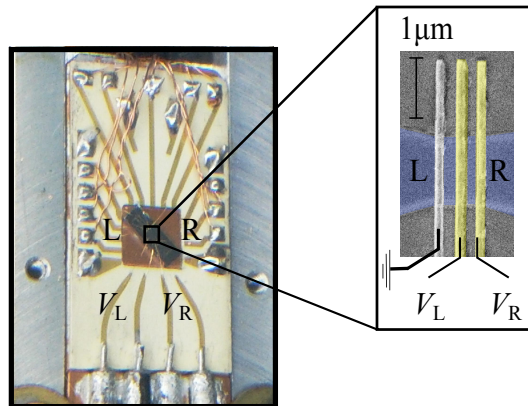


FIG. 4. Radio frequency sample holder with sample and a scanning electron microscope image of its surface (same image as in Fig. 1(a) of the main article).

with a gold plated copper surface thermally connected to the mixing chamber of a dilution refrigerator at a base temperature of $\simeq 50$ mK. The control gates used to define the QD barriers (yellow gates in the detailed sample view in Fig. 4, the gray gate is grounded) are connected to stainless steel rf coax cables. Source and drain contacts are connected via standard constantan wires and low pass filtered at room temperature. All cables are heat sunked at several points in the cryostat. A simplified sketch of the device circuit highlighting the capacitive control is presented in Fig. 5.

Calibration measurements

Our numerical calculations rely on accurate measurements of the QD characteristics including the relevant energy scales, capacitive coupling constants, tunnel rates and realistic line broadening. In the following we present our calibration measurements. We begin by showing in Fig. 6 a typical single dot stability diagram depicting the current I through the QD as a function of the voltage applied to the left gate V_L and the source-drain voltage V . Note that varying the right instead of the left gate would result in a comparable plot. The white dots along the $V = 0$ horizontal indicate the positions of current maxima in Fig. 1 of the main article. As expected, they are located at the crossings of the Coulomb diamonds at $V = 0$. From the dimensions of the Coulomb diamonds (horizontal and vertical arrows) we estimate the

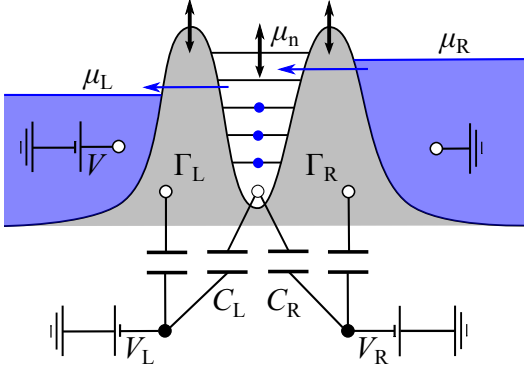


FIG. 5. Sketch of the QD circuit. Tunnel rates, $\Gamma_{L,R}$, and dot levels μ_n (horizontal lines) are capacitively controlled by the gate voltages, V_L and V_R . The leads contain a degenerate electron system with chemical potentials, $\mu_{L,R}$. The current is measured at the grounded right lead, while the voltage $V = (\mu_R - \mu_L)/e$ is applied on the left lead. For $V > 0$ electrons tunnel via QD levels with $\mu_R \geq \mu_n \geq \mu_L$ from the right to the left lead (blue arrows).

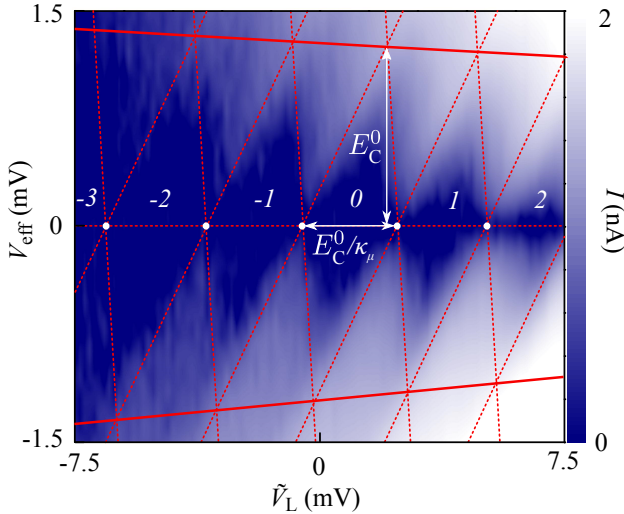


FIG. 6. Calibration of charging energies and gate voltages to energy conversion. Gate voltages are not modulated. Plotted is the current through the QD measured as a function of gate voltage $\tilde{V}_L = V_L + 202 \text{ mV}$ and bias V_{eff} at constant $\tilde{V}_R = V_R + 91 \text{ mV} = -2.5 \text{ mV}$. The numbers indicate our index parameter n . White dots mark the corresponding current maxima positions in Fig. 1a of the main article. Red lines illustrate the Coulomb blockade diamonds.

charging energies $E_C(n) = e^2/C_{\text{QD}}(n)$ and the capacitive coupling $\kappa_\mu = eC_{L,R}(n)/C_{\text{QD}}(n)$, where $C_{\text{QD}}(n)$ is the eigen capacitance of the QD [at the working point $C_L^0 \simeq C_R^0 \simeq 50 \text{ aF}$ and $C_{\text{QD}}^0 \simeq 130 \text{ aF}$]. We find an approximate linear dependence $E_C(n) = E_C^0 + n\delta E$ with $\delta E = -0.04 \text{ meV}$ and at the working point $E_C^0 = 1.27 \text{ meV}$ (solid lines in Fig. 6) and an approximately con-

stant leverage factor $\kappa_\mu = 0.38e$. Thus, the gate voltages shift the chemical potentials of the resonances as $\mu_n(\tilde{V}_L, \tilde{V}_R) = \mu_n^0 + \epsilon_0(\tilde{V}_L, \tilde{V}_R)$ with $\mu_n^0 = \mu_n(0, 0)$ and the onsite energy

$$\epsilon_0(\tilde{V}_L, \tilde{V}_R) = -\kappa_\mu(\tilde{V}_L + \tilde{V}_R). \quad (3)$$

The above relations can be reinterpreted as $\mu_n = nE_C^0 - n(n+1)\delta E/2 + \mu_n^0(n=0)$, where $\mu_n^0(n=0) = 0.41 \text{ meV}$ is the difference between the chemical potential of grounded leads and that of the lowest unoccupied dot-level at $\tilde{V}_L = \tilde{V}_R = 0$. The influence of the gate voltages on the dot-lead tunnel rates can be estimated from the dc current shown in Fig. 1(a) of the main text. In Fig. 7, we plot these data along the bisecting line $\tilde{V}_L = \tilde{V}_R$ of

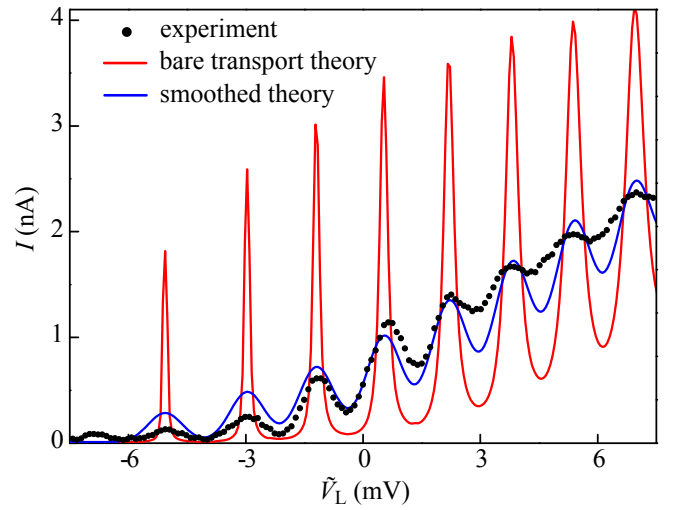


FIG. 7. Calibration of tunnel couplings. Current through the QD for $V = 100 \mu\text{V}$, data from Fig. 1 along its bisecting line where $V_L = V_R$ and $\Gamma_L \simeq \Gamma_R$ (black dots). Also shown are two theory curves, all using $\kappa_\Gamma = 0.03e$, $\Gamma = 0.13 \text{ meV}$ in Eq. (4), charging energies from Table I and assuming $\Gamma_L = \Gamma_R$: $e\Gamma_{L,R}/h$ according to Eq. (4) current calculated with standard scattering theory with finite tunnel barriers as only broadening mechanism (red solid line), see Eq. (9) and below; calculated current as above but additionally convoluted with a Gaussian inhomogeneous distribution of constant width mimicing slow charge noise (blue line).

Fig. 1(a). The Coulomb blockade oscillations display current maxima, but their smoothed average exhibits an exponential dependence on gate voltages below the working point $\tilde{V}_L = \tilde{V}_R = 0$ devolving into a linear increase above. To capture this averaged behavior with only two free parameters, we assume the dependence as

$$\Gamma_\alpha(\tilde{V}_\alpha) = \frac{\kappa_\Gamma \tilde{V}_\alpha}{1 - \exp(-\kappa_\Gamma \tilde{V}_\alpha/\Gamma)}, \quad (4)$$

where $\alpha = L, R$, while $\Gamma \equiv \Gamma_L^0 = \Gamma_R^0 = 0.13 \text{ meV}$ is the tunnel coupling at the working point and $\kappa_\Gamma \simeq 0.03e$ is

TABLE I. Experimentally determined parameters of our QD; from left to right: index number n , chemical potentials at the working point $\tilde{V}_L = \tilde{V}_R = 0$, charging energies $E_C(n) = \mu_n - \mu_{n-1}$, tunnel couplings for the case of symmetric coupling $\Gamma_L = \Gamma_R$ and $\tilde{V}_L = \tilde{V}_R$ such that $\mu_n = 0$, i.e., $\Gamma_{L,R} = \Gamma_\alpha(\mu_n^0/2\kappa_\mu)$, see Eqs. (3) and (4).

| n | μ_n^0 (meV) | $E_C(n)$ (meV) | $\Gamma_{L,R}$ (meV) at $\mu_n = 0$ |
|-----|-----------------|----------------|-------------------------------------|
| -3 | -3.85 | 1.39 | 0.39 |
| -2 | -2.25 | 1.35 | 0.59 |
| -1 | -0.90 | 1.31 | 0.82 |
| 0 | 0.41 | 1.27 | 1.09 |
| 1 | 1.68 | 1.23 | 1.40 |
| 2 | 2.91 | 1.19 | 1.74 |
| 3 | 4.11 | 1.15 | 2.13 |
| 4 | 5.31 | 1.11 | 2.53 |

the slope for large \tilde{V}_L, \tilde{V}_R . The red solid line in Fig. 7 represents the prediction from Eq. (9) below based on scattering theory including the finite couplings $\Gamma_L(V) = \Gamma_R(V)$ as only broadening mechanism [discussed below Eq. (9)]. Convoluting this curve with an additional Gaussian broadening of constant width yields a better fit to the measured data (blue line). The Gaussian expresses an inhomogeneous broadening caused by slow statistical fluctuations of the QD levels (charge noise). In our case this inhomogeneous broadening is the dominant broadening mechanism. The non-perfect fit is likely a consequence of the increasing relevance of dissipation as the barriers open up. Note that the values of $\Gamma_L(V) = \Gamma_R(V)$ are predetermined by the integral of the current peaks which is independent of additional inhomogeneous broadening. In Table I we summarize the functional dependences along the bisecting line in Fig. 1(a) of the main article according to the equations above.

Radio frequency calibration — proof of adiabaticity

Next, we discuss the calibration of the amplitude of the radio frequency gate voltage modulation. Figure 8 demonstrates an apparent problem of our non-perfect rf setup, namely strong cable resonances, i.e. standing waves caused by reflections of the rf-signal at the sample holder and meters away at the rf generator. In the adiabatic regime we expect to find a pump current $|I| \propto f$, if $V = 0$. Instead we observe strong current oscillations which indicate an oscillating modulation amplitude even though the rf signal strength is fixed, the main reason being cable resonances. For our ratchet experiments we restricted ourselves to specific modulation frequencies, namely $f = 25, 50, 100, 150, 200$ MHz. In Fig. 9 we demonstrate exemplarily for one of the gates the calibration of the modulation amplitude at these frequencies. Plotted is the differential conductance of the QD as function of V_R and its modulation amplitude V_R^{rf} (where

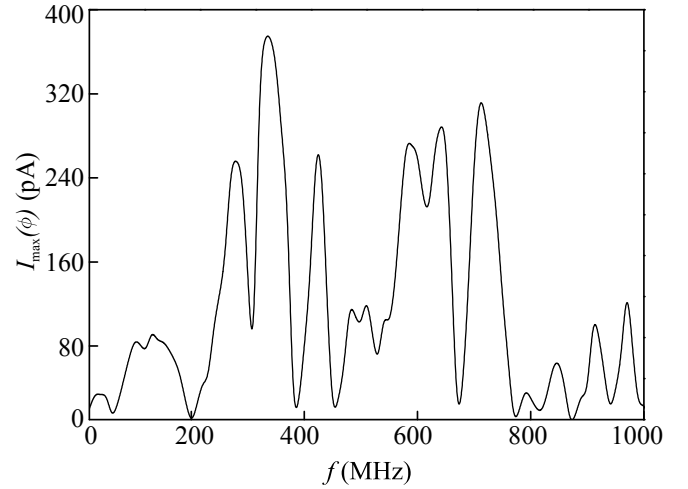


FIG. 8. Maximum current I_{max} for phase difference ϕ from 0 to 2π through the unbiased QD plotted as a function of modulation frequency at $k = 1$ and modulation amplitude $A = 3E_C^0$.

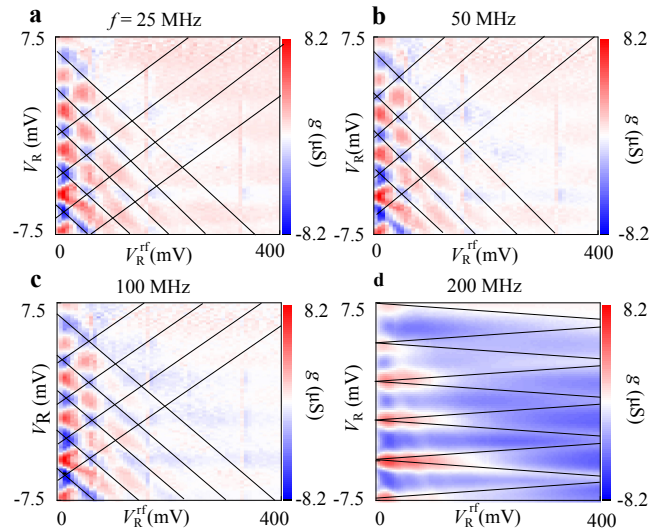


FIG. 9. Radio frequency calibrations of the right hand side gate for $f = 25, 50, 100, 200$ MHz in panels a-d. Plotted is the differential conductance $g = dI/dV$ as a function of applied modulation voltage V_R^{rf} and mean gate voltage V_R (at constant $V_L = -90$ mV). The flocks of parallel black lines with mutually opposite slopes are guide for the eyes indicating current resonances which depart proportional to the increasing amplitude.

$V_R(t) = V_R + V_R^{\text{rf}} \cos 2\pi f t$) while the left gate voltage is kept constant. Each Coulomb resonance splits in two resonances located at the turn around points of $V_R(t)$. These splittings are proportional to V_R^{rf} and are indicated by black lines in Fig. 9. Their slopes $\alpha_R(f) = V_R/V_R^{\text{rf}}$ can be used to calibrate the actual rf modulation amplitude

TABLE II. Radio frequency calibration factors $\alpha_{L,R}$ at various driving frequencies.

| f in MHz | $1/\alpha_L$ | $1/\alpha_R$ |
|------------|--------------|--------------|
| 25 | 25.2 | 24.9 |
| 50 | 23.2 | 23.1 |
| 100 | 27.5 | 27.2 |
| 150 | 26.3 | 26.1 |
| 200 | 182.5 | 178.6 |

according to:

$$A_{L,R} = \kappa_\mu \alpha_{L,R}(f) V_{L,R}^{\text{rf}} / e \quad (5)$$

The result of the calibration (of both gates) is summarized in Table II. To account for the frequency dependent calibration in our measurements we correct the amplitudes at each frequency according to Table II and Eq. (5). In Fig. 10(a) we present $I(\phi)$ at four frequencies for $k = 1$

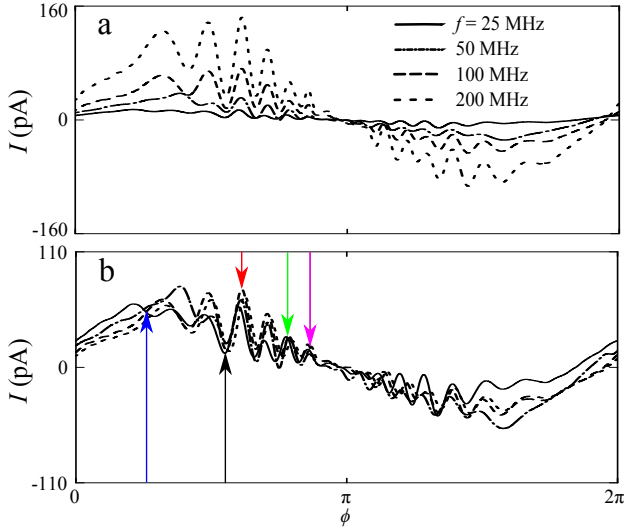


FIG. 10. (a) Current I as a function of phase difference ϕ for $k = 1$, and $A = 3E_C^0$. The current has been corrected for the frequency dependent transfer functions of the cables by applying the calibration factors $\alpha_{L,R}(f)$ listed in Table II according to Eq. (5). (b) Same data as in panel a but scaled by $I(f) \rightarrow \frac{100 \text{ MHz}}{f} I(f)$.

and identical modulation amplitudes $A = 3E_C^0$ after calibration. The same data scaled by $I(f) \rightarrow \frac{100 \text{ MHz}}{f} I(f)$ to the current expected at $f = 100$ MHz are approximately frequency independent [Fig. 10(b)]. It demonstrates not only the validity of our procedure to calibrate the rf amplitudes but also corroborates our assumption of adiabatic charge transport. Small deviations, especially those near $\phi = 0$ are probably related to a local disorder potential which compromises the spacial symmetry. The importance of a correct calibration becomes evident in Fig. 11 plotting I_{max} in direct comparison to the uncalibrated current taken from Fig. 8. Straight lines are guide for the eyes indicating the adiabatic transport regime.

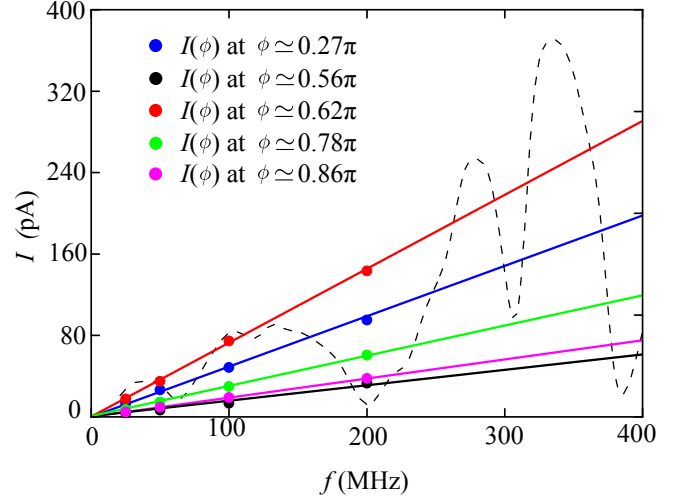


FIG. 11. Frequency dependence of current before and after calibration of the modulation amplitude. The dashed line presents uncalibrated data identical to those in Fig. 8. Colored symbols indicate current values of specific maxima and minima (constant phase) marked in Fig. 10(a) by arrows; same as in the inset of Fig. 1(b) of the main paper. The straight lines are a guide for the eyes and verify the expected adiabatic regime.

Theoretical approach

We derive a scattering formalism for the dc current through a periodically driven conductor in the low-frequency limit, which generalizes the scattering approach for parametric pumping [15, 16] to the presence of a finite dc voltage and a tiny ac bias. The derivation starts from Floquet scattering theory [12, 17–19] which we expand for a small driving frequency $f = \Omega/2\pi$. Despite that we will finally apply the approach to a two-terminal device, we formulate the general theory for an arbitrary number of leads.

A cornerstone of Floquet scattering theory is an expression for the probability $T_{\alpha\beta}(t, \epsilon)$ that an electron with initial energy ϵ from lead β is scattered to lead α at time t . Then the time-dependent net current in lead α can be expressed as [12, 19]

$$I_\alpha = \frac{e}{h} \int d\epsilon \left[f(\epsilon - \tilde{\mu}_\alpha(t)) - \sum_\beta T_{\alpha\beta}(t, \epsilon) f(\epsilon - \tilde{\mu}_\beta(t)) \right], \quad (6)$$

where $h = 2\pi\hbar$ denotes Planck's constant while $f(x) = [\exp(x/k_B T) + 1]^{-1}$ is the Fermi function for thermal energy $k_B T$. In our experiment, the modulation of the gate voltages induces a tiny ac bias caused by a tiny capacitance between the modulated gates and the electrical leads of the QD. To capture this, we allow for periodically time-dependent chemical potentials $\tilde{\mu}_\alpha(t) = \mu_\alpha + ew_\alpha(t)$. Our goal is to derive a convenient expression for the time-average of $I_\alpha(t)$ in the adiabatic limit.

We start by Taylor expansion of the Fermi functions in the ac shift $w_\alpha(t)$. It yields the time-dependent current $G_{\alpha\beta}(t)w_\beta(t)$ with the time-periodic conductance matrix

$$G_{\alpha\beta}(t) = G_{\alpha\beta}(\vec{v}(t)) = \frac{e^2}{h} [\delta_{\alpha\beta} - T_{\alpha\beta}(t, \bar{\mu})]. \quad (7)$$

Despite that the ac bias $w_\beta(t)$ vanishes on average, its impact becomes rectified and contributes

$$I_\alpha^{\text{rect}} = \int_0^T \frac{dt}{T} G_{\alpha\beta}(\vec{v}(t)) w_\alpha(t) \quad (8)$$

to the dc measured current, where T is the modulation period.

Having considered the ac bias, we now come to the effects of a dc voltage and the modulation of tunnel barriers and the QD levels. We employ ideas put forward in Refs. [18, 20, 21]. For the now constant chemical potentials, the time-average of the transmission $T_{\alpha\beta}(t, \epsilon)$ provides $T_{\alpha\beta}^{(k)}(\epsilon)$, which is the probability that an electron with initial energy ϵ coming from lead β is scattered to lead α after the absorption of k energy quanta, where negative k corresponds to emission. Thus, the final energy of the electron is $\epsilon + k\hbar\Omega$. Then the net average current flowing from lead β to the conductor assumes the intuitive form [12, 17–19]

$$I_\alpha = \frac{e}{h} \int d\epsilon \left[f(\epsilon - \mu_\alpha) - \sum_{\beta, k} T_{\alpha\beta}^{(k)}(\epsilon) f(\epsilon - \mu_\beta) \right]. \quad (9)$$

This expression can be derived from a time-dependent wire-lead model which relates the transmission to the scattering matrix and the Green's function of the driven conductor [12, 18, 22]. From the unitarity of the scattering matrix follows charge conservation, which means that an electron with initial energy ϵ will be scattered with probability unity to any sideband k in any lead α , so that the sum over all these channels must fulfill the relation

$$\sum_{\alpha, k} T_{\alpha\beta}^{(k)}(\epsilon) = 1. \quad (10)$$

With the same arguments but summing over all initial states that end up with energy ϵ in lead α we obtain a further sum rule:

$$\sum_{\beta, k} T_{\alpha\beta}^{(k)}(\epsilon - k\hbar\Omega) = 1. \quad (11)$$

Adiabatic limit

We have performed experiments in the adiabatic limit corresponding to an expansion of I_α to first order in Ω . For the Taylor expansion we insert the left-hand side of

Eq. (11) as prefactor of $f(\epsilon - \mu_\alpha)$ into the current formula (9) and obtain

$$I_\alpha = \sum_{\beta, k} \frac{e}{h} \int d\epsilon \left\{ T_{\alpha\beta}^{(k)}(\epsilon) [f(\epsilon - \mu_\alpha) - f(\epsilon - \mu_\beta)] - k\hbar\Omega \frac{\partial T_{\alpha\beta}^{(k)}(\epsilon)}{\partial \epsilon} f(\epsilon - \mu_\alpha) \right\}. \quad (12)$$

Notice that in contrast to Ref. [18], we have expanded in Ω for the transmission rather than for the Fermi function, so that the result holds whenever the transmission as a function of ϵ is smooth on the scale $\hbar\Omega$. In particular, it is valid also for low temperature, i.e. beyond the high-temperature limit of $k_B T \gg \hbar\Omega$.

Next we make use of the time-periodicity of the driving which has the consequence that the propagator $U(t, t - \tau)$ depends not only on the difference τ , but explicitly on both the initial time $t - \tau$ and the final time t . After Fourier transformation with respect to τ , one obtains both the propagator and the scattering matrix for an electron with initial energy ϵ [12]. The result is periodic in time and can be written as

$$S(t, \epsilon) = S(t + T, \epsilon) = \sum_k e^{-ik\Omega t} S^{(k)}(\epsilon). \quad (13)$$

Then from the usual relation between transmission amplitudes and probabilities, $T_{\alpha\beta}(t, \epsilon) = |S_{\alpha\beta}(t, \epsilon)|^2$, and taking the time-average of the current follows $T_{\alpha\beta}^{(k)}(\epsilon) = |S_{\alpha\beta}^{(k)}(\epsilon)|^2$. [Notice that generally the transmission to the k th sideband, $T_{\alpha\beta}^{(k)}(\epsilon)$, is different from the k th Fourier coefficient of $T_{\alpha\beta}(t, \epsilon)$]. Next we employ Parseval's theorem to write the k -summation in Eq. (12) as time-integration over one driving period. Moreover, it is convenient to define voltages V_α as deviations from an average chemical potential, $\mu_\alpha = \bar{\mu} + eV_\alpha$, and evaluate the Fermi functions for zero temperature and small voltage. Then we end up with the time-averaged current

$$I_\alpha = \sum_\beta \bar{G}_{\alpha\beta} V_\beta + I_\alpha^{\text{rect}} + \frac{Q_\alpha^{\text{cycle}}}{T}, \quad (14)$$

with the time averaged conductance

$$\bar{G}_{\alpha\beta} = \int_0^T \frac{dt}{T} G_{\alpha\beta}(\vec{v}(t)) \quad (15)$$

and the current resulting from the rectified ac bias given in Eq. (8). The last term in Eq. (14) reflects the charge parametrically pumped through contact α during one driving period,

$$Q_\alpha^{\text{cycle}} = \frac{1}{2\pi} \text{Im} \int_0^T dt \left(S(t, \mu_\alpha) \frac{\partial}{\partial t} S^\dagger(t, \mu_\alpha) \right)_{\alpha\alpha}. \quad (16)$$

The shape of the driving can be expressed by a closed curve \mathcal{C} in parameter space, $\vec{v}(t) = \vec{v}(t + T)$. Then, if \mathcal{C}

is traversed adiabatically slowly, the scattering matrix depends merely parametrically on time, i.e. $S(t, \epsilon) = S(\vec{v}(t), \epsilon)$, where the latter is the static result for the instantaneous value of \vec{v} at time t . This allows one to transform the time integral in Eq. (16) to a closed line integral to obtain

$$Q_\alpha^{\text{cycle}} = \frac{1}{2\pi} \text{Im} \oint_{\mathcal{C}} d\vec{v} \cdot (S(\vec{v}, \mu_\alpha) \text{grad} S^\dagger(\vec{v}, \mu_\alpha))_{\alpha\alpha}. \quad (17)$$

Applying Stokes' theorem, one can transfer this expression into a surface integral to obtain Brouwer's formula [16]. For the numerical evaluation in the parameter range considered here, however, the present form is more appropriate.

An important implication of Eq. (14) is the separation of the average current into a dc contribution stemming from the average conductance and an adiabatically pumped charge. The main difference between these two quantities is their behavior under time inversion of the closed curve \mathcal{C} : While the average conductance is invariant, the pumped charge acquires a minus sign. Below, we will explore this symmetry property for the Lissajous curves applied in the experiment.

Independent channel approximation

In our experiment, the conductor is formed by a QD connecting two leads, $\alpha = L, R$. It is driven with an amplitude A ranging from zero to the rather large value $5E_C^0$, so that the onsite energy of the QD may change by several charging energies—we will consider up to 10 excess electrons. Moreover, the influence of the gate voltage applied to the tunnel barriers turns out to be crucial for the observed pumping, so that a master equation approach based on lowest-order perturbation theory in the dot-lead coupling is not appropriate. As a consequence, already for the static transport problem, a full treatment that includes all possible spin and correlation effects is practically impossible. We instead assume that each charge state of the quantum dot contributes as independent transport channel to the current. This requires that the separation of the resonances given by the charging energy is larger than their homogeneous widths such that the conductance peaks are well separated. Moreover, the driving must be slow enough that the quantum dots can be assumed to be always relaxed to its many-particle ground state. Our QD model is parametrized by the energies μ_n necessary for adding the next electron to the QD. Thus, the position of the corresponding conductance peak is directly related to μ_n . Assuming that all these peaks are well separated, we can treat the resonances as independent levels that can be occupied by a spinless electron. The corresponding scattering matrices

read

$$S_n(\epsilon) = \mathbf{1} - \frac{i}{\epsilon - \mu_n + i(\Gamma_L + \Gamma_R)/2} \begin{pmatrix} \Gamma_L & \sqrt{\Gamma_L \Gamma_R} \\ \sqrt{\Gamma_L \Gamma_R} & \Gamma_R \end{pmatrix}, \quad (18)$$

where Γ_L and Γ_R are the dot-lead tunnel rates.

We drive our QD by applying time-dependent gate voltages to the tunnel barriers. Thus these gate voltages form our parameter space and are the components of the vector $\vec{v}_{k,\phi}(t) \equiv [\tilde{V}_L(t), \tilde{V}_R(t)]$, see Eq. (1) of the main article. They entail a time-dependence on the onsite energy ϵ_0 and thus on μ_n as well as on the dot-lead tunnel rates Γ_L and Γ_R . For the onsite energy, we assume the linear relation (3). The height of each tunnel barrier is also shifted approximately linearly by the respective gate voltage. For ideal tunnel barriers according to the WKB formula, one would expect that the dot-lead tunnel rates depend exponentially on the gate voltages. Our dc measurements, however, indicate that this overestimates the rates for large positive $V_{L,R}$. Therefore, we assume for $\Gamma_\alpha(\vec{v})$ the dependence given by Eq. (4) with $\Gamma \equiv \Gamma_L^0 = \Gamma_R^0 = 0.07 \text{ meV}$ and $\kappa_\Gamma \simeq 0.03$. In order to evaluate the current formula (14), we insert the scattering matrix S_n into Eqs. (15) and (17) and subsequently sum the contribution of the resonances n .

Even though this approach already allows us to obtain the dc current (all our numerical results are computed in this way), it is instructive to investigate the contribution of a single resonance to both the average conductance and the charge per cycle. For this purpose, we assume that at a resonance, the dot-lead rates are weakly time-dependent with average values $\bar{\Gamma}_{L,R}$, while $\mu_n(t) \simeq (t - t_0)\dot{\mu}_n$. Then the straightforward evaluation of Eq. (15) with the off-diagonal matrix element of S_n yields

$$\bar{G}^n \simeq \frac{e^2}{h} \frac{\bar{\Gamma}_L \bar{\Gamma}_R}{\bar{\Gamma}_L + \bar{\Gamma}_R} \frac{\Omega}{|\dot{\mu}_n|} \quad (19)$$

Notice that $\dot{\mu}_n$ is proportional to Ω and, thus, \bar{G}^n is frequency independent.

The pumped charge is essentially determined by the scattering phase in the prefactor of S_n . Assuming again that the $\bar{\Gamma}_{L,R}$ are practically constant at the resonance, we find [21]

$$Q_L^n \simeq \frac{e\bar{\Gamma}_L}{\bar{\Gamma}_L + \bar{\Gamma}_R} \text{sign}(\dot{\mu}_n). \quad (20)$$

This means that for $\bar{\Gamma}_L \gg \bar{\Gamma}_R$, an electron enters from or leaves to the left lead depending on the sign of $\dot{\mu}_n$. In the opposite limit, the right lead is relevant and Q_L^{res} is much smaller than the elementary charge. This also emphasizes the role of the parameter dependence of the tunnel rates: In the derivation of Eq. (20), we assumed that the $\Gamma_{L,R}$ stays constant when a level crosses the chemical potential of a lead at time $t = t_0$. However, in a complete pump cycle, the level will cross the chemical potential as many

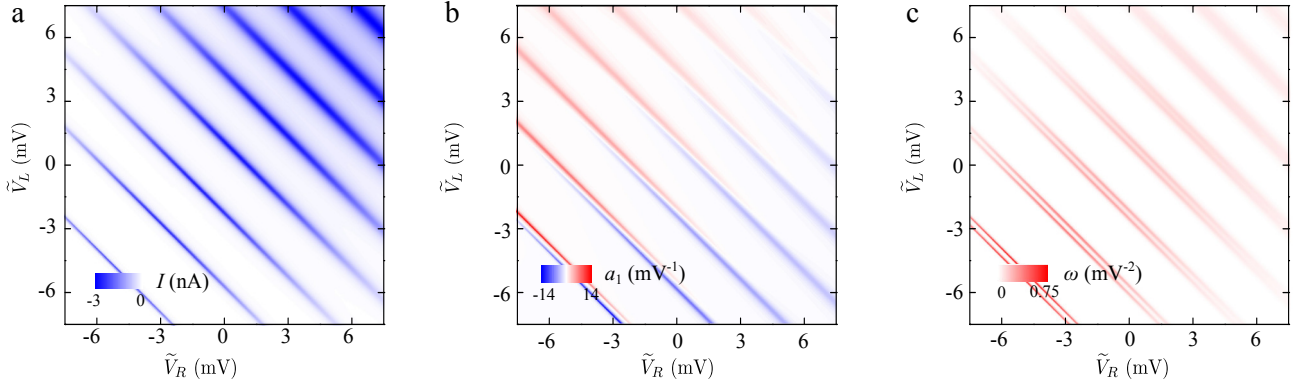


FIG. 12. (a) Current in the absence of the modulation for bias voltage $V = 200\text{mV}$. (b) Component $a_1(\vec{v})$ of the vector field (21) appearing in the symmetrized line integral representation of the charge pumped per cycle. Positive values (blue stripes, marked with +) emerge when a QD level equals the chemical potential of the left lead and correspond to electron pumping from the left lead to the QD. Accordingly, the curvature is negative (red, -) when a QD level agrees with the chemical potential of the right lead, while the mismatch stems from the voltage bias. In the relevant regime, the second component, $a_2(\vec{v})$, looks very similar. (c) Corresponding curvature $\omega = (\partial a_1/\partial x_2 - \partial a_2/\partial v_1)$ that appears in the symmetrized Brouwer's formula. The lines are splitted due to the bias.

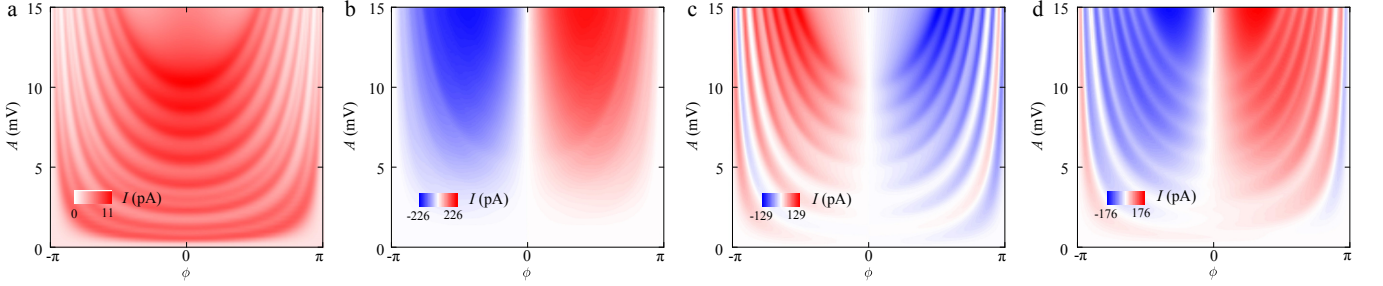


FIG. 13. Theoretical prediction of the current for $k = 1$ shown in Fig. 1(b) of the main article, $f_L = f_R = 200\text{MHz}$. The dc tunnel current $\bar{G}V$ (a), the pumped current $Q^{\text{cycle}}f$ (b), and the ac current (c) sum up to the total current plotted in (d).

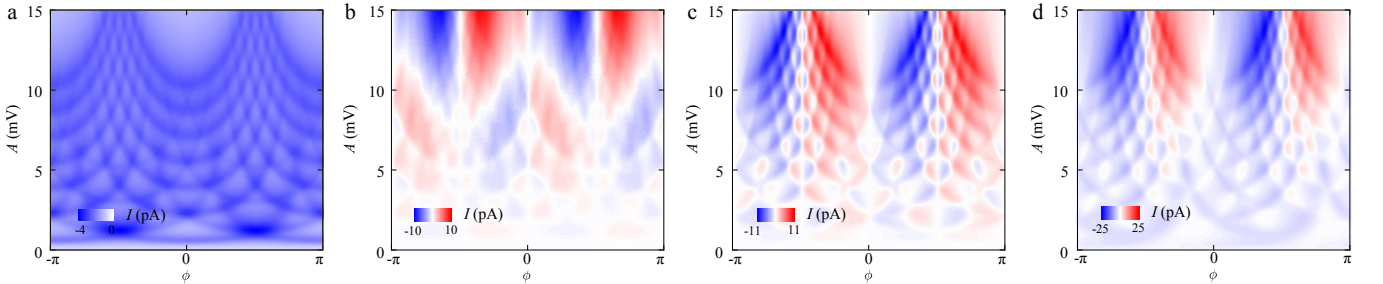


FIG. 14. Theoretical prediction of the current for $k = 2$ shown in Fig. 2(a) of the main article, $f_L = 50\text{MHz}$ $f_R = 100\text{MHz}$. The dc tunnel current $\bar{G}V$ (a), the pumped current $Q^{\text{cycle}}f$ (b), and the ac current (c) sum up to the total current plotted in (d).

times from above as it crosses from below. Thus if $\Gamma_{L,R}$ were constant, the net charge pumped from the left lead to the dot in the whole cycle would vanish. In turn, we will observe significant pumping from the left lead to the right lead if $\Gamma_L \gg \Gamma_R$ when the dot level is lowered, while $\Gamma_L \ll \Gamma_R$ when the level is raised.

For a two-terminal device, the pumped currents entering the dot from the left and from the right lead compen-

sate each other so that $Q_L^{\text{cycle}} + Q_R^{\text{cycle}} = 0$. Nevertheless, the vector fields appearing in the integral in Eq. (17) may differ by more than their sign, because the integrands are relevant only up to a gradient field which vanishes under the closed line integral. Therefore it is more convenient to discuss the integrand of the symmetrized expression for the pumped charge: $Q^{\text{cycle}} = \frac{1}{2}(Q_L^{\text{cycle}} - Q_R^{\text{cycle}}) =$

$\oint_{\mathcal{C}} d\vec{v} \cdot a(\vec{v})$ with the vector field

$$\vec{a} = \frac{i}{4\pi} \sum_n \left\{ (S_n \text{grad } S_n^\dagger)_{\text{LL}} \Big|_{\mu_{\text{L}}} - (S_n \text{grad } S_n^\dagger)_{\text{RR}} \Big|_{\mu_{\text{R}}} \right\}. \quad (21)$$

Figure 12(b) shows the first component of $\vec{a}(\vec{v})$ for the parameters of our quantum dot. A significant contribution requires that the resonant level lies close to the chemical potential of a lead. For small bias, this is also a necessary condition for the emergence of a conductance peak, see Fig. 12(a). To make direct use of Brouwer's formula, one would transform via Stokes' theorem the line integral into a surface integral [see remark after Eq. (17)] and would end up with an integration over the curvature shown in Fig. 12(c).

Lissajous pumping and symmetries

The gate voltages applied in the experiment follow Lissajous curves in parameter space defined as

$$\vec{v}_{k,\phi}(t) = \begin{pmatrix} \tilde{V}_{\text{L}}(t) \\ \tilde{V}_{\text{R}}(t) \end{pmatrix} = A \begin{pmatrix} \cos(\Omega t - \phi) \\ \cos(k\Omega t) \end{pmatrix}, \quad (22)$$

where henceforth k is referred to as order and ϕ is the phase shift between the two components. Driving the two barriers with different but commensurate frequencies is a particular feature of our experiment. The amplitude A is equal at both barriers and is typically several E_{C}^0 in our experiments. A central question is that of the symmetry properties of the dc conductance and the pumped charge as a function of the modulation parameters.

We start our symmetry considerations by noticing that the Lissajous figures obey $\vec{v}_{k,\phi}(t) = \vec{v}_{k,\phi+2\pi/k}(t+2\pi/k\Omega)$, namely that a phase shift of $2\pi/k$ is canceled by a time shift of $2\pi/k\Omega$. This implies that the dc current patterns, being averaged over time, as a function of ϕ possess a k -fold symmetry in ϕ .

A further symmetry property of the three contributions to the current in Eq. (14) follows from the behavior of $\bar{G}_{\alpha\beta}$, Q^{cycle} , and I^{rect} under time reversal. It plays a crucial role for adiabatic pumping [16] and ratchet effects. Below, we find $2k$ symmetry points at which $\bar{G}_{\alpha\beta}$ is symmetric, while Q^{cycle} and I^{rect} are anti-symmetric under time reversal. For a derivation, we determine for each Lissajous curve $\vec{v}_{k,\phi}$ a time-reversed partner with phase ϕ' which must fulfill the condition

$$\vec{v}_{k,\phi}(t) = \vec{v}_{k,\phi'}(-t + t_0), \quad (23)$$

for all times t . The inversion $t \rightarrow -t$ is thereby accompanied by a time offset t_0 , which is permitted by the time periodicity of the integrands in Eqs. (8), (15), and (17). Inserting Eq. (22) into Eq. (23) yields $\Omega t_0 = 2\pi\ell/k$ and $\phi' = -\phi + 2\pi(\ell/k + \ell')$ where $\ell = 0, 1, \dots, k-1$

and $\ell' = 0, 1$. The special phases $\phi_{\ell\ell'} = \pi(\ell/k + \ell')$ fulfill $\phi = \phi'$ (with t_0 given above), so that the original and the time-reversed Lissajous curves [defined by Eq. (22)] lie on top of each other, while they evolve in opposite direction in time. Thus, the phases $\phi_{\ell\ell'}$ define $2k$ in-equivalent points with TRS. An interesting observation is that there, the Lissajous curve takes the form $\tilde{V}_{\text{R}}(\tilde{V}_{\text{L}}) = \pm \cos[k \arccos(\pm \tilde{V}_{\text{L}})]$. This defines the k th Chebyshev polynomial [23] which represents a degenerate loop that does not enclose a finite area. As a consequence, Q^{cycle} and I^{rect} (with odd symmetry under time-reversal) vanish. Hence, at the symmetry points the current takes the value $\bar{G}V$ and, in particular, vanishes for $V = 0$.

Substituting in Eq. (22) the phase ϕ by the deviation from the symmetry point, $\Delta\phi = \phi - \phi_{\ell\ell'}$, one can see that time reversal corresponds to $\Delta\phi \rightarrow -\Delta\phi$. Thus, the behavior of the integrals in Eqs. (8), (15), and (17) under time reversal allows us to draw conclusions about the symmetries of $\bar{G}_{\alpha\beta}$ and Q^{cycle} as a function of $\Delta\phi$. To be specific: Since the average conductance Eq. (15) is invariant under time reversal, it must be an even function of $\Delta\phi$. By contrast, the charge pumped per cycle, Eq. (17), changes its sign upon time reversal. Consequently, it must be an odd function of $\Delta\phi$. In short, despite the only k -fold symmetry of the Lissajous curves Eq. (22), we find $2k$ in-equivalent phases at which $\bar{G}_{\alpha\beta}$ is symmetric, while Q^{cycle} is anti-symmetric.

Our experimental results indicate that the rf modulation of gate voltages induces a tiny ac bias. Its origin is a tiny capacitive coupling between the modulated gates and the 2D leads of the QD. Therefore, we model it as modulation of the chemical potentials $\tilde{\mu}_\alpha(t) = \mu_\alpha + ew_\alpha(t)$ with a phase shift of $-\pi/2$ compared to the modulation of the gate voltages [described in Eq. (1) of the main article]:

$$\vec{w}_{k,\phi}(t) = \begin{pmatrix} w_{\text{L}}(t) \\ w_{\text{R}}(t) \end{pmatrix} = \kappa_{\text{ac}} A \begin{pmatrix} \sin(\Omega t - \phi) \\ \sin(k\Omega t) \end{pmatrix}. \quad (24)$$

The capacitive coupling constant κ_{ac} turns out to be of the order $5 \cdot 10^{-4}$ and is expected to decrease with the modulation frequency, $\kappa_{\text{ac}} \propto \Omega^{-1}$.

In comparison to the gate voltages in Eq. (22), the ac modulation of the chemical potentials, \vec{w} , contains a sine instead of a cosine. In a symmetry analysis along the lines above, this finally leads to a minus sign. Therefore the integrand in Eq. (8) is an odd function of t (besides a time shift by t_0), so that the rectified current changes its sign under time reversal. Consequently, I^{rect} is anti-symmetric in $\Delta\phi$.

In Figs. 13 and 14, we show for $k = 1, 2$ the three contribution to the current in Eq. (2) of the main text, i.e., the dc current $\bar{G}V$, the pump current $Q^{\text{cycle}}f$, and the contribution of the rectified ac bias, I^{rect} . This visualizes the symmetry of the dc current and the anti-symmetry of the second and the third contribution. Notably, for

the case of a tiny dc voltage of $V = 1\mu\text{V}$ considered here, the overall behavior [panel (d)] is dominated by the anti-symmetric contributions.

Additional data

In Fig. 15 we compare the measured Lissajous ratchet data for $k = 1, 2, 3$ also discussed in the main article but all in spherical coordinates and add another data set for $k = 4$. The data contain the predicted $k + 1$ -fold symmetry but also show a complex detailed structure caused by the combination of the three contributions in Eq. (2) of the main article, namely the time averaged conductance $\bar{G}V$, the ratchet current $Q^{\text{cycle}}f$ and I^{rect} . It is possible to reduce the information in similar measurements, such that the $k + 1$ -fold symmetry is more evident, by increasing the dot-lead tunnel couplings. We do this by shifting the working point to the mixed valance regime where the Coulomb current peaks overlap strongly ($\tilde{V}_L = 12.5\text{mV}$ and $\tilde{V}_R = 12.5\text{mV}$, see Fig. 1(a) of the main article). The result is a strong broadening which thoroughly washes out most fine structure of the current. In Fig. 16 we present such data up to $k = 3$. These measurement are a clear demonstration of the Lissajous ratchet effect as they emphasize the symmetry properties of Q^{cycle} .

Applications and alternative realizations

In our Lissajous rocking ratchet a combination of rf excitations breaks the time reversal symmetry and yields a dc current. It represents a new method to access radio frequency information by mutually comparing the frequencies, amplitudes and phases of rf signals. As such, Lissajous rocking ratchets could find applications as rf comparator or serve as detector or filter components. Our quantum dot implementation is interesting for quantum information processing applications, as it allows one to compare and process small rf-signal on-chip. In a simplified picture a Lissajous ratchet resembles an on-chip rf Lock-In amplifier: to illustrate this idea imagine that we apply a clean rf reference to one gate and a noisy signal to the second gate. The resulting dc current strongly depends on the relative phase, amplitude and frequency of the two signals. By measuring a time averaged dc current, our device filters the time periodic carrier signal while averaging out uncorrelated noise, just as a Lock-In amplifier does. However, the Lissajous ratchet allows a detailed comparison of mutual rf-signals going well beyond the scope of a Lock-In amplifier.

Lissajous rocking ratchets are not limited to QD circuits but could be realized in a variety of systems, for instance in macroscopic electronics or mechanics or in superconducting circuits. In the following we propose a possible realization in a nanoelectromechanical systems.

In Fig. 17 we extend the already realized “nano bell” [24] and illustrate what we mean by “nanomechanical Newton cradle”. The device is composed of two cantilevers and a fixed metallic contact (R). The central cantilever is patterned with an isolated metallic island while the left one contains an island but electrically connected to a second lead (L). The islands are positioned such, that the central island can touch both the left and right leads whenever both cantilevers are vibrating with sufficiently high amplitude. A voltage can be applied between L and R and current can be measured. We assume that both cantilevers can be externally driven (at predefined relative phases) at their mutual eigen frequencies and that the latter are tunable, e.g., via capacitive coupling to additional gates or by using dielectric forces [25]. We also assume that the central island is small enough to allow for single electron transport based on Coulomb blockade, namely that we can treat it as a QD [24]. The electronic levels of the islands are then modulated by the same capacitive coupling that is used to mechanically drive the cantilevers. In such a device the coupling between the islands and that between contact R and the center island are strongly time dependent, zero most of the time and strong during touching. This system is highly tunable and very close in spirit to our QD circuit: importantly, the time dependence of the couplings and island levels are linked, a central precondition to define a Lissajous ratchet.

* Present address: Paul-Drude-Institut für Festkörperelektronik, Hausvogteiplatz 5–7, 10117 Berlin, Germany

- [1] R. P. Feynman, R. B. Leighton, and M. Sands, *The Feynman Lectures on Physics*, Vol. 1 (Addison Wesley, Reading MA, 1963) Chap. 46.
- [2] P. Reimann, Phys. Rep. **361**, 57 (2002).
- [3] V. S. Khrapai, S. Ludwig, J. P. Kotthaus, H. P. Tranitz, and W. Wegscheider, Phys. Rev. Lett. **97**, 176803 (2006).
- [4] P. Hänggi and F. Marchesoni, Rev. Mod. Phys. **81**, 387 (2009).
- [5] Y. Ono and Y. Takahashi, App. Phys. Lett. **82**, 1221 (2003).
- [6] X. Jehl, B. Voisin, T. Charron, P. Clapera, S. Ray, B. Roche, M. Sanquer, S. Djordjevic, L. Devoille, R. Wacquez, and M. Vinet, Phys. Rev. X **3**, 021012 (2013).
- [7] L. P. Kouwenhoven, A. T. Johnson, N. C. van der Vaart, C. J. P. M. Harmans, and C. T. Foxon, Phys. Rev. Lett. **67**, 1626 (1991).
- [8] M. D. Blumenthal, B. Kaestner, L. Li, S. Giblin, T. J. B. M. Janssen, M. Pepper, D. Anderson, G. Jones, and D. A. Ritchie, Nature Phys. **3**, 343 (2007).
- [9] B. Kaestner, V. Kashcheyevs, S. Amakawa, M. D. Blumenthal, L. Li, T. J. B. M. Janssen, G. Hein, K. Pierz, T. Weimann, U. Siegner, and H. W. Schumacher, Phys. Rev. B **77**, 153301 (2008).
- [10] See Supplemental Material for details.
- [11] H. Linke, W. Sheng, A. Lofgren, H. Xu, P. Omling, and

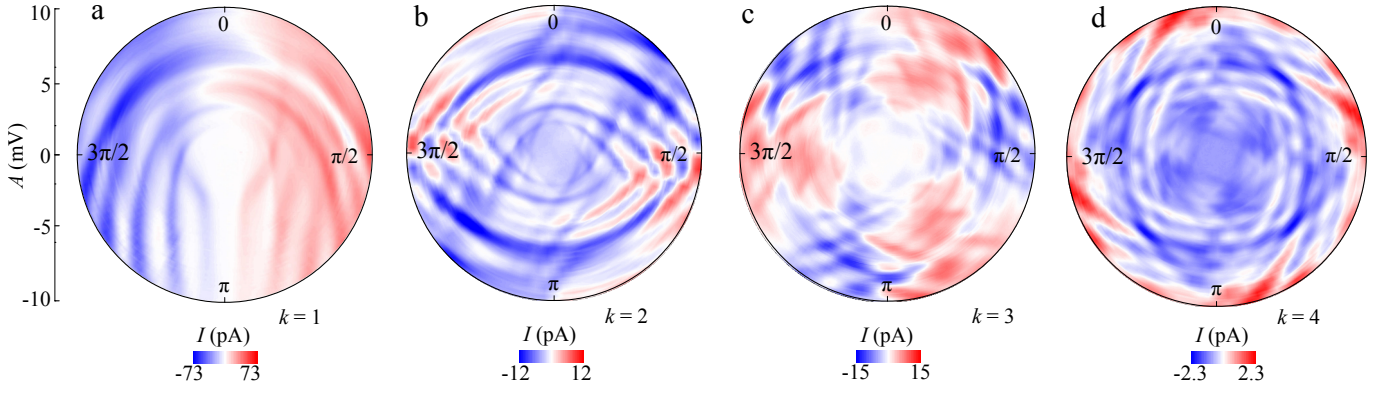


FIG. 15. Measured current I versus modulation amplitude and phase for (a) $k = 1$ and $f_L = f_R = 100$ MHz, (b) $k = 2$ and $f_L = 100$ MHz $f_R = 200$ MHz, (c) $k = 3$ and $f_L = 50$ MHz $f_R = 150$ MHz, (d) $k = 4$ and $f_L = 50$ MHz $f_R = 200$ MHz. The data for $k = 3$ are identical to those in Fig. 2 of the main article. The working point is defined by $V_L = -202$ mV and $V_R = -91$ mV as marked in Fig. 1(a) of the main article.

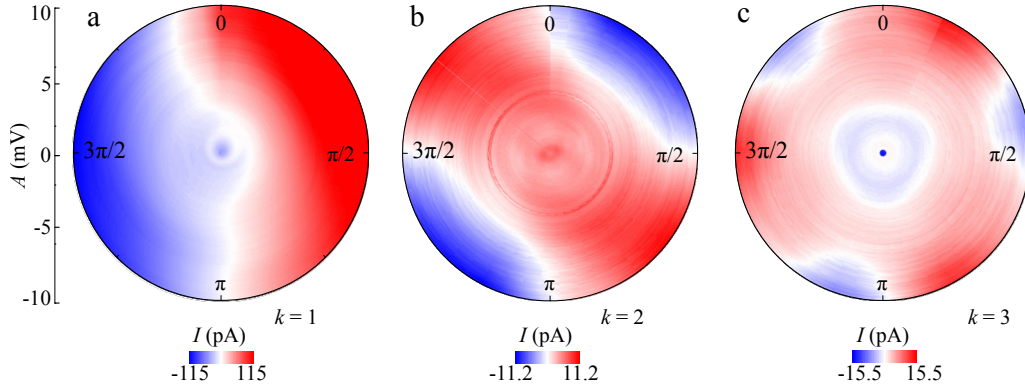


FIG. 16. Measured current I versus modulation amplitude and phase for (a) $k = 1$ and $f_L = f_R = 100$ MHz, (b) $k = 2$ and $f_L = 50$ MHz $f_R = 100$ MHz, (c) $k = 3$ and $f_L = 50$ MHz $f_R = 150$ MHz. The working point is defined by $\tilde{V}_L = 12.5$ mV and $\tilde{V}_R = 12.5$ mV near the upper right corner of Fig. 1(a) of the main article. The enhanced dot-lead tunnel coupling washes out most fine structures compared to the data in Fig. 15 above.

- [12] S. Kohler, J. Lehmann, and P. Hänggi, Phys. Rep. **406**, 379 (2005).
- [13] F. Forster, G. Petersen, S. Manus, P. Hänggi, D. Schuh, W. Wegscheider, S. Kohler, and S. Ludwig, Phys. Rev. Lett. **112**, 116803 (2014).
- [14] S. P. Giblin, M. Kataoka, J. D. Fletcher, P. See, T. J. B. M. Janssen, J. P. Griffiths, G. A. C. Jones, I. Farrer, and D. A. Ritchie, J. Appl. Phys. **114**, 164505 (2013).
- [15] A. Prêtre, H. Thomas, and M. Büttiker, Phys. Rev. B **54**, 8130 (1996).
- [16] P. W. Brouwer, Phys. Rev. B **58**, R10135 (1998).
- [17] M. Wagner and F. Sols, Phys. Rev. Lett. **83**, 4377 (1999).
- [18] M. Moskalets and M. Büttiker, Phys. Rev. B **66**, 205320 (2002).
- [19] S. Camalet, J. Lehmann, S. Kohler, and P. Hänggi, Phys. Rev. Lett. **90**, 210602 (2003).
- [20] O. Entin-Wohlman, A. Aharony, and Y. Levinson, Phys. Rev. B **65**, 195411 (2002).
- [21] V. Kashcheyevs, A. Aharony, and O. Entin-Wohlman, Phys. Rev. B **69**, 195301 (2004).
- [22] N. S. Wingreen, A.-P. Jauho, and Y. Meir, Phys. Rev. B **48**, 8487 (1993).
- [23] I. M. Gradshteyn and I. S. Ryzhik, *Table of Integrals, Series, and Products*, 5th ed. (Academic Press, San Diego, 1994).
- [24] D. R. Koenig, E. M. Weig, and J. P. Kotthaus, Nature Nano. **3**, 482 (2008).
- [25] Q. P. Unterreithmeier, E. M. Weig, and J. P. Kotthaus, Nature **458**, 1001 (2009).

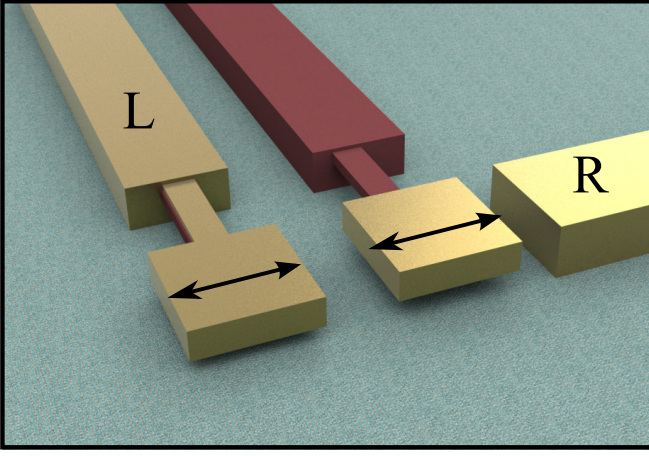


FIG. 17. Nanomechanical Newton cradle discussed in the main text.